Computational Materials Science 71 (2013) 115–123

Contents lists available at SciVerse ScienceDirect

Computational Materials Science

journal homepage: www.elsevier.com/locate/commatsci

Experimental and numerical investigation for ductile fracture of Al-alloy 5052 using modified Rousselier model

Junhang Guo [a,b], Shengdun Zhao [a], Ri-ichi Murakami [b,*], Shunlai Zang [a]

[a] School of Mechanical Engineering, Xi'an Jiaotong University, No. 28, Xianning West Road, Xi'an, Shaanxi 710049, China
[b] Department of Mechanical Engineering, The University of Tokushima, 2-1, Minami-Josanjima, Tokushima 770-8506, Japan

ARTICLE INFO

Article history:
Received 18 September 2012
Received in revised form 24 December 2012
Accepted 9 January 2013

Keywords:
Constitutive equation
Finite element method
Aluminum alloy
Ductile fracture
Lode parameter

ABSTRACT

In this paper, the ductile fracture of Al-alloy 5052 is studied by experiments and simulations using a modified Rousselier model. Although tension failure has been successfully predicted by the classical Rousselier model, its predictive capability on shear failure was seldom discussed. A modified Rousselier model was proposed by incorporating the recent extended damage evolution model by Nahshon and Hutchinson. The modified Rousselier model can capture both tension and shear failure. A stress integration algorithm based on the general backward-Euler return algorithm for this constitutive model was developed and implemented into finite element model by the user defined material subroutine VUMAT in the ABAQUS/Explicit. The tensile tests of smooth round bar and notched round bars with different sizes were carried out to investigate the mechanical behavior of Al-alloy 5052. Consequently, the material parameters of the classical Rousselier model were identified by an inverse method using these experimental data. A shear test was also performed to calibrate the new shear damage coefficient in the modified Rousselier model. For the shear test, the simulations show that although shear failure can be predicted by the Rousselier model, the ductility was over-estimated. However, the modified Rousselier model can give more accurate results. The simulations on uniaxial tension of the round bars also confirm that the modified Rousselier model can well predict the cup-cone fracture mode. The results indicate that the Lode parameter in the new damage evolution model is important to capture the cup-cone fracture mode transition.

1. Introduction

It is well known that when metal fractures, microvoids will experience a complex process, including the nucleation, growth and coalescence. In order to describe this damage and fracture process, many ductile fracture models using local approaches have been published. In the view of macroscopic phenomenology, the Gurson model in [1] developed well in the past decades. The calibration methods for Gurson model were proposed [2,3] and it was widely used in the prediction of ductile fracture in [4–6].

The mean stress $\sigma_m = \sigma_{kk}/3$ and effective stress $\sigma_{eq} = (3\underline{\sigma}_d : \underline{\sigma}_d/2)^{1/2}$ play important roles in ductile fracture [1], but the relation between the effective plastic strain at fracture and the stress triaxiality ($\eta = \sigma_m/\sigma_{eq}$) is not generally monotonic [7,8]. Also, some experiments in [9] show that the ductility and fracture mechanism of metals is also influenced by the Lode parameter. More and more tests show that the damage in material is influenced by shear deformation as well as tension [10,11]. But the void evolution function used in Gurson's model showed limitations in recent years for its inapplicability to localization and fracture for low triaxiality or shear-dominated deformations [12]. So, a non-dimensional metric of stress $\omega(\underline{\sigma})$ was recommended to discriminate between axisymmetric and shear-dominated stress states in [12]. And then an extension of the damage growth function was proposed which incorporates damage growth under low triaxiality such as shear-dominated state [12]. The modified Gurson model was utilized to simulate quasi-static punch-out tests of high ductility DH36 steel in [13]. In [14], a whole calibration procedure for this model was given using a finite element (FE)-based inverse method. The predictive capability of the modified Gurson model was evaluated in [15,16] by a series of experiments and simulations. In [17], a shear void nucleation term based on the Lode parameter for plastic strain rate is used to model slant fracture by Morgeneyer and Besson. In [18], Li et al. research shows that the applicability of the ductile fracture criteria depends on the use of suitable damage evolution rules and consideration of several influential factors, including the Lode parameter, etc.

After Rousselier published his damage model based on continuum damage mechanics in [19–21], some numerical computational methods and simulations have been done in [22–32], aimed at proposing robust and reliable FE formulations and developing this model to a non-local and mesh independent model, etc. The recent research on the Rousselier model in [23] shows that the

* Corresponding author. Tel./fax: +81 88 656 7392.
E-mail address: murakami@tokushima-u.ac.jp (R.-i. Murakami).

0927-0256/$ - see front matter © 2013 Elsevier B.V. All rights reserved.
http://dx.doi.org/10.1016/j.commatsci.2013.01.011

cup-cone fracture mode in tension test of notched round bar can be predicted. In [30,31], the Rousselier model's predictive applicability under shear deformation was mentioned but has not been assessed yet. In this paper, the capability of the Rousselier model is assessed and it is shown that some modifications on damage evolution are required.

2. Modified Rousselier model

In this section, a brief introduction of the Rousselier model is given and followed by its modification. Rousselier developed the simplest possible model of porous metal plasticity in the framework of thermodynamics of irreversible processes in [19]. The material's isotropy and elastic-plasticity with isotropic hardening are assumed in this model. Two internal variables are used to quantify the deterioration process of material, one is the equivalent plastic strain p and the other is the so-called damage variable or void volume fraction f. The Rousselier damage model includes yield potential, stress strain relation, normality rule, and the evolution of damage variable. The yield potential is written as Eq. (1), so it is a coupled constitutive equation in which the damage accumulation and hydrostatic stress are incorporated.

$$\Phi = \frac{\sigma_{\text{eq}}}{\rho} - R(p) + Df\sigma_1 \exp\left(\frac{\sigma_m}{\rho\sigma_1}\right) = 0 \tag{1}$$

where $\underline{\underline{\sigma}} = \underline{\underline{\sigma}}_d + \sigma_m \underline{\underline{I}}$ is the Cauchy stress tensor, $\underline{\underline{\sigma}}_d$ is the deviatoric tress tensor, σ_m is hydrostatic stress, $\underline{\underline{I}}$ is the second order unity tensor, $\sigma_{eq} = (3\underline{\underline{\sigma}}_d : \underline{\underline{\sigma}}_d/2)^{1/2}$ is the von Mises equivalent stress, $\rho = (1-f)/(1-f_0)$ is the relative density, f is the damage variable or void volume fraction, f_0 is the initial void volume fraction in the material, $R(p)$ is the hardening function of the material, $p = (2\underline{\underline{\varepsilon}}^p_d : \underline{\underline{\varepsilon}}^p_d/3)^{1/2}$ is the equivalent plastic strain, D and σ_1 are Rousselier material constants, usually $D = 2$ [18–20]. The stress strain relation or Hooke's Law is written as the following equation:

$$\underline{\underline{\sigma}} = \rho\underline{\underline{\underline{\underline{E}}}} : \underline{\underline{\varepsilon}}^e = \rho\underline{\underline{\underline{\underline{E}}}} : (\underline{\underline{\varepsilon}} - \underline{\underline{\varepsilon}}^p) \tag{2}$$

where $\underline{\underline{\underline{\underline{E}}}}$ is the elastic modulus tensor, $\underline{\underline{\varepsilon}}$ is the strain tensor, $\underline{\underline{\varepsilon}}^e$ and $\underline{\underline{\varepsilon}}^p$ are the elastic and plastic part of strain tensor respectively. Using the normality rule, the plastic strain rate tensor can be expressed as Eq. (3).

$$\dot{\underline{\underline{\varepsilon}}}^p = \dot{p}\frac{\partial\Phi}{\partial(\underline{\underline{\sigma}}/\rho)} = \dot{p}\left[\frac{3\underline{\underline{\sigma}}_d}{2\sigma_{eq}} + \frac{1}{3}Df\exp\left(\frac{\sigma_m}{\rho\sigma_1}\right)\underline{\underline{I}}\right] \tag{3}$$

It is remarkable that the plastic part of strain tensor can be divided into the deviatoric part and volumetric part by $\underline{\underline{\varepsilon}}^p = \underline{\underline{\varepsilon}}^p_d + \varepsilon^p_m \underline{\underline{I}}$, therefore, the deviatoric part of plastic strain rate tensor can be given as:

$$\dot{\underline{\underline{\varepsilon}}}^p_d = \dot{p}\frac{3\underline{\underline{\sigma}}_d}{2\sigma_{eq}} \tag{4}$$

And the volumetric plastic strain rate was derived as the following equation:

$$\dot{\varepsilon}^p_m = \frac{1}{3}\dot{p}Df\exp\left(\frac{\sigma_m}{\rho\sigma_1}\right) \tag{5}$$

The relation between the damage variable with the volumetric plastic strain rate used in Rousselier model was derived by mass conservation as the following equation:

$$\dot{f} = 3(1-f)\dot{\varepsilon}^p_m \tag{6}$$

By substituting Eq. (5) into Eq. (6), the evolution rate of the damage variable can be written as a function of the equivalent plastic strain rate and mean stress:

$$\dot{f} = Df(1-f)\exp\left(\frac{\sigma_m}{\rho\sigma_1}\right)\dot{p} \tag{7}$$

According to Nahshon and Hutchinson in [12], the void growth is no longer directly tied to the plastic volume change as it is in the original model, and simply treated as a parameter measuring the damage accumulation in the material. It is recommended that the void evolution rate can be written as Eq. (8) with an additional phenomenological term. It results in a maximum effect for pure shear and no effect for axisymmetric stress states.

$$\dot{f} = 3(1-f)\dot{\varepsilon}^p_m + k_\omega f\omega(\underline{\underline{\sigma}})\frac{\underline{\underline{\sigma}}_d\dot{\underline{\underline{\varepsilon}}}^p_d}{\sigma_{eq}} \tag{8}$$

Here k_ω is the shear damage coefficient, which sets the magnitude of the void coalescence rate in shear deformation [12–16]. And the invariant measure $\omega(\underline{\underline{\sigma}})$ is given by

$$\omega(\sigma) = 1 - \xi^2 = 1 - \left(\frac{27J_3}{2\sigma^3_{eq}}\right)^2 \tag{9}$$

$$J_3 = \det(\underline{\underline{\sigma}}_d) = (\sigma_I - \sigma_m)(\sigma_{II} - \sigma_m)(\sigma_{III} - \sigma_m) \tag{10}$$

Here $\xi = \frac{27J_3}{2\sigma^3_{eq}}$ is the Lode parameter in [18], or normalized third invariant in [16] and lies in the range $-1 \leqslant \omega \leqslant 1$, J_3 is the third stress invariant of the deviatoric tress tensor $\underline{\underline{\sigma}}_d$, σ_I, σ_{II} and σ_{III} are the principal stresses of the tress tensor $\underline{\underline{\sigma}}$ and are assumed to be ordered as $\sigma_I \geqslant \sigma_{II} \geqslant \sigma_{III}$. The non-dimensional metric in Eq. (9) lies in the range $0 \leqslant \omega \leqslant 1$ to discriminate between axisymmetric and shear-dominated stress states. For all axisymmetric stress states, $\omega = 0$. And for all states comprised of a pure shear stress plus a hydrostatic contribution, $\omega = 1$ (see details in [12]). Here, the Lode angle θ could be introduced as Eq. (11), which is the same definition as in [10].

$$\cos(3\theta) = \frac{27J_3}{2\sigma^3_{eq}} \tag{11}$$

Then the relation between the non-dimensional metric $\omega(\underline{\underline{\sigma}})$ and the Lode angle could be introduced as

$$\omega(\underline{\underline{\sigma}}) = \sin^2(3\theta) \tag{12}$$

Substitute Eqs. (4) and (5) into Eq. (8), then a new damage evolution rule could be derived as the following equation:

$$\dot{f} = \left[Df(1-f)\exp\left(\frac{\sigma_m}{\rho\sigma_1}\right) + k_\omega f\omega(\underline{\underline{\sigma}})\right]\dot{p} \tag{13}$$

When elasticity is neglected, the mean stress $\sigma_m = 0$, and $\omega(\underline{\underline{\sigma}})$ keeps as constant, Eq. (13) can be transferred to an ordinary differential equation

$$\frac{df}{dp} = Df(1-f) + k_\omega\omega(\underline{\underline{\sigma}})f \tag{14}$$

With f_0 as the initial void volume fraction, the analytical solution can be derived as:

$$f = \frac{(D + k_w\omega(\underline{\underline{\sigma}}))f_0}{(D + k_w\omega(\underline{\underline{\sigma}}) - Df_0)e^{-(D+k_w\omega(\underline{\underline{\sigma}}))p} + Df_0} \tag{15}$$

Then for the shear stress state, the solution can be particularized with $D = 2$, and $\omega(\underline{\underline{\sigma}}) = 1$ as

$$f = \frac{(2 + k_w)f_0}{(2 + k_w - 2f_0)e^{-(2+k_w)p} + 2f_0} \tag{16}$$

By substituting $f_0 = 10^{-4}$ and different $k_w = 0.0, 0.5, 1.0, 1.5$ into Eq. (15), the evolution of damage variable with respect to the equivalent plastic strain p can be obtained as Fig. 1. It can be seen

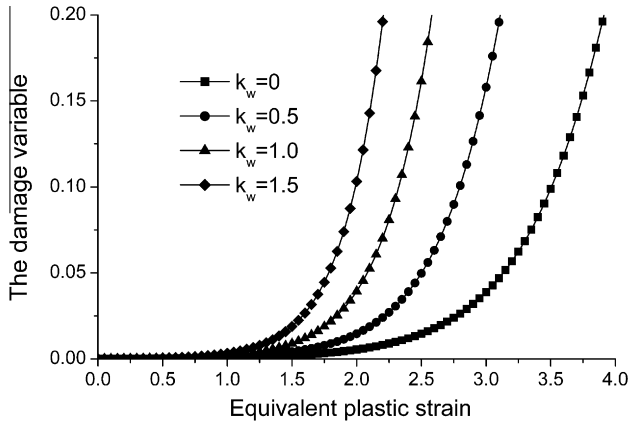

Fig. 1. The damage variable evolutions with respect to the equivalent plastic strain p under pure shear. The analytical solutions are obtained with the initial void volume fraction $f_0 = 10^{-4}$ and different shear damage coefficient $k_\omega = 0.0, 0.5, 1.0, 1.5$ respectively.

that, for the original Rousselier model ($k_w = 0$), the damage variable increases with the equivalent plastic strain p even in shear deformation as shown in the following equation:

$$f = \frac{f_0}{(1-f_0)e^{-2p} + f_0} \tag{17}$$

Here, it should be noted one of the differences between Gurson and Rousselier models. With Gurson model, no void growth is obtained in pure shear. However, with Rousselier model, the void growth can be obtained in pure shear as presented in Fig. 1. The additional phenomenological term in Eq. (8) could be considered as a nucleation term and not as a void growth term, because it does not comply with the mass conservation law.

3. Numerical implementation of stress integration algorithm

The stress integration algorithm is developed and discussed in this section. The general return-mapping algorithm for plasticity established in [13,33–35] is a good choice, for its higher accuracy and unconditional stability. Although a backward-Euler algorithm was first proposed for the model by Rousselier in [36] and Lorentz et al. in [23] respectively, the stress integration algorithm for the modified Rousselier model is briefly developed as following within this framework and employed in FE models.

According to [33,34], from a computational standpoint the plasticity problem can always be regarded as strain-driven. So, in this framework, it can be supposed that the internal variables $\underline{\underline{\sigma}}_t, f_t, p_t$ are given at time t, the purpose of the stress integration algorithm is to update them to $\underline{\underline{\sigma}}_{t+\Delta t}, f_{t+\Delta t}, p_{t+\Delta t}$ by strain increment $\Delta\underline{\underline{\varepsilon}}$. Firstly, suppose that the strain increment is a purely elastic process and the trail stress $\underline{\underline{\sigma}}^{tr}$ can be obtained by Eq. (2), which is determined by Hooke's Law as

$$\underline{\underline{\sigma}}^{tr} = \underline{\underline{\sigma}}_t + \rho_t \underline{\underline{\underline{\underline{E}}}} : \Delta\underline{\underline{\varepsilon}} = \underline{\underline{\sigma}}_t + \rho_t(\lambda Tr(\Delta\underline{\underline{\varepsilon}})\underline{\underline{I}} + 2G\Delta\underline{\underline{\varepsilon}}) \tag{18}$$

Here λ is the bulk modulus, G is the shear modulus. Next, the yield surface is used to determine whether the strain increment is elastic or not. If $\Phi = \frac{\sigma^{tr}_{eq}}{\rho_t} - R(p_t) + Df_t\sigma_1 \exp\left(\frac{\sigma^{tr}_m}{\rho_t\sigma_1}\right) < 0$, then it is an elastic process and $\underline{\underline{\sigma}}_{t+\Delta t} = \underline{\underline{\sigma}}_t, f_{t+\delta t} = f_t, p_{t+\Delta t} = p_t$. But if $\Phi \geqslant 0$, it is an elastic–plastic process and the increment of the strain consists of plastic strain part. Then the backward-Euler return algorithm is employed to calculate the increment of plastic flow multiplier δp. Arrange Eq. (3) as

$$\dot{\underline{\underline{\varepsilon}}}^p_d = \dot{p}\frac{3\underline{\underline{\sigma}}_d}{2\sigma_{eq}} = \dot{p}\frac{\partial\sigma_{eq}}{\partial\underline{\underline{\sigma}}_d} \tag{19}$$

And arrange Eq. (1) as

$$\Phi = \sigma_{\mathrm{eq}}\frac{1-f_0}{1-f} - \mathrm{R}(p) + Df\sigma_1\exp\left(\frac{\sigma_m}{\sigma_1}\frac{1-f_0}{1-f}\right) = 0 \tag{20}$$

Suppose there is an increment of plastic strain $\delta\underline{\underline{\varepsilon}}^p_d$ then the decomposition of strain increment can be rewritten as:

$$\begin{aligned}\Delta\underline{\underline{\varepsilon}} &= \Delta\underline{\underline{\varepsilon}}^e + \Delta\underline{\underline{\varepsilon}}^p_d + \Delta\varepsilon^p_m\underline{\underline{I}} \\ &= \Delta\underline{\underline{\varepsilon}}^e - \delta\underline{\underline{\varepsilon}}^e + \Delta\underline{\underline{\varepsilon}}^p_d + \delta\underline{\underline{\varepsilon}}^p_d + \Delta\varepsilon^p_m\underline{\underline{I}} + \delta\varepsilon^p_m\underline{\underline{I}}\end{aligned} \tag{21}$$

Then the plastic strain increment can be updated by flow rule using the second-order Taylor expansion:

$$\begin{aligned}\Delta\underline{\underline{\varepsilon}}^p_d &= \Delta\underline{\underline{\varepsilon}}^p_d + \delta\underline{\underline{\varepsilon}}^p_d = (\Delta p + \delta p)\frac{\partial\sigma_{eq}\left(\underline{\underline{\sigma}} - \delta\underline{\underline{\sigma}}\right)}{\partial\underline{\underline{\sigma}}} \\ &\approx (\Delta p + \delta p)\left(\frac{\partial\sigma_{eq}}{\partial\underline{\underline{\sigma}}} - \frac{\partial^2\sigma_{eq}}{\partial\underline{\underline{\sigma}}^2} : \delta\underline{\underline{\sigma}}\right) \\ &\approx \Delta p\frac{\partial\sigma_{eq}}{\partial\underline{\underline{\sigma}}} + \delta p\frac{\partial\sigma_{eq}}{\partial\underline{\underline{\sigma}}} - \Delta p\frac{\partial^2\sigma_{eq}}{\partial\underline{\underline{\sigma}}^2} : \delta\underline{\underline{\sigma}}\end{aligned} \tag{22}$$

The total volumetric plastic strain increment can also be updated as

$$\Delta\varepsilon^p_m = \Delta\varepsilon^p_m + \delta\varepsilon^p_m = \Delta\varepsilon^p_m + \frac{\partial\varepsilon^p_m}{\partial p}\delta p \tag{23}$$

Here

$$\frac{\partial\varepsilon^p_m}{\partial p} = \frac{1}{3}Df\exp\left(\frac{\sigma_m - \delta\sigma_m}{\rho\sigma_1}\right) \tag{24}$$

Then the stress increment can be written as

$$\Delta\underline{\underline{\sigma}} - \delta\underline{\underline{\sigma}} = \rho\underline{\underline{\underline{\underline{E}}}} : (\Delta\underline{\underline{\varepsilon}} - \Delta\underline{\underline{\varepsilon}}^p) = \rho\underline{\underline{\underline{\underline{E}}}} : (\Delta\underline{\underline{\varepsilon}} - \Delta\underline{\underline{\varepsilon}}^p_d - \Delta\varepsilon^p_m\underline{\underline{I}}) \tag{25}$$

Substitute Eqs. (22) and (23) into Eq. (25) to get the stress increment as

$$\begin{aligned}\Delta\underline{\underline{\sigma}} - \delta\underline{\underline{\sigma}} &= \rho\underline{\underline{\underline{\underline{E}}}} : (\Delta\underline{\underline{\varepsilon}} - \Delta\underline{\underline{\varepsilon}}^p_d - \Delta\varepsilon^p_m\underline{\underline{I}}) = \rho\underline{\underline{\underline{\underline{E}}}} : \\ &\times\left(\Delta\underline{\underline{\varepsilon}} - \Delta p\frac{\partial\sigma_{eq}}{\partial\underline{\underline{\sigma}}} - \delta p\frac{\partial\sigma_{eq}}{\partial\underline{\underline{\sigma}}} + \Delta p\frac{\partial^2\sigma_{eq}}{\partial\underline{\underline{\sigma}}^2} : \delta\underline{\underline{\sigma}} - \Delta\varepsilon^p_m\underline{\underline{I}} - \frac{\partial\varepsilon^p_m}{\partial p}\delta p\underline{\underline{I}}\right)\end{aligned} \tag{26}$$

Then the stress increment can be written as

$$\delta\underline{\underline{\sigma}} = Q^{-1}r_b \tag{27}$$

Here

$$Q = \underline{\underline{I}} + \rho\Delta p\underline{\underline{\underline{\underline{E}}}} : \frac{\partial^2\sigma_{eq}}{\partial\underline{\underline{\sigma}}^2} \tag{28}$$

And the so-called residual vector

$$r_b = \Delta\underline{\underline{\sigma}} - \rho\underline{\underline{\underline{\underline{E}}}} : \left(\Delta\underline{\underline{\varepsilon}} - \Delta p\frac{\partial\sigma_{eq}}{\partial\underline{\underline{\sigma}}} - \delta p\frac{\partial\sigma_{eq}}{\partial\underline{\underline{\sigma}}} - \Delta\varepsilon^p_m\underline{\underline{I}} - \frac{\partial\varepsilon^p_m}{\partial p}\delta p\underline{\underline{I}}\right) \tag{29}$$

Then according to consistency condition

$$\Phi(\underline{\underline{\sigma}} - \delta\underline{\underline{\sigma}}, f + \delta f, \Delta p + \delta p) = 0 \tag{30}$$

Using the first-order Taylor expansion gives

$$r_\phi - \frac{\partial\phi}{\partial\sigma}\delta\sigma + \frac{\partial\phi}{\partial f}\delta f + \frac{\partial\phi}{\partial p}\delta p = 0 \tag{31}$$

Here

$$r_\Phi = \left(\frac{\underline{\underline{\sigma}}}{\rho}\right)_{eq} - \mathrm{R}(p) + Df\sigma_1 \exp\left(\frac{\sigma_m}{\rho\sigma_1}\right) \tag{32}$$

$$\frac{\partial \Phi}{\partial \underline{\underline{\sigma}}} = \frac{1}{\rho}\frac{\partial \sigma_{eq}}{\partial \underline{\underline{\sigma}}} + \frac{Df}{3\rho}\exp\left(\frac{\sigma_m}{\rho\sigma_1}\right)\underline{\underline{I}} \tag{33}$$

$$\frac{\partial \Phi}{\partial f}\delta f = \frac{\partial \Phi}{\partial f}\frac{\partial f}{\partial p}\delta p \tag{34}$$

$$\frac{\partial \Phi}{\partial f} = \sigma_{\mathrm{eq}}\frac{1-f_0}{(1-f)^2} + D\sigma_1\left(1 + f\frac{1-f_0}{(1-f)^2}\right)\exp\left(\frac{\sigma_m}{\sigma_1}\frac{1-f_0}{1-f}\right) \tag{35}$$

$$\frac{\partial f}{\partial p} = (1-f)Df\exp\left(\frac{\sigma_m}{\rho\sigma_1}\right) + k_\omega f\omega(\underline{\underline{\sigma}}) \tag{36}$$

$$\frac{\partial \Phi}{\partial p} = -\frac{\partial R(p)}{\partial p} \tag{37}$$

Then the increment of plastic flow multiplier:

$$\delta p = \frac{r_\Phi - \frac{\partial \Phi}{\partial \underline{\underline{\sigma}}} : Q^{-1} : \left[\Delta\underline{\underline{\sigma}} - \rho\underline{\underline{\underline{\underline{E}}}} : \left(\Delta\underline{\underline{\varepsilon}} - \Delta p\frac{\partial \sigma_{eq}}{\partial \underline{\underline{\sigma}}} - \Delta\varepsilon_m^p\underline{\underline{I}}\right)\right]}{\frac{\partial \Phi}{\partial \underline{\underline{\sigma}}} : Q^{-1} : \rho\underline{\underline{\underline{\underline{E}}}} : \left(\frac{\partial \sigma_{eq}}{\partial \underline{\underline{\sigma}}} + \frac{\partial \varepsilon_m^p}{\partial p}\underline{\underline{I}}\right) - \frac{\partial \Phi}{\partial f}\frac{\partial f}{\partial p} + \frac{\partial R(p)}{\partial p}} \tag{38}$$

And finally the process is repeated according to Eqs. (39)–(41) to satisfy the consistency condition.

$$\Delta\underline{\underline{\sigma}}_{t+\Delta t} = \Delta\underline{\underline{\sigma}}_t - \delta\underline{\underline{\sigma}} \tag{39}$$

$$\Delta p_{t+\Delta t} = \Delta p_t + \delta p \tag{40}$$

$$f_{t+\Delta t} = f_t + \frac{\partial f}{\partial p}\delta p \tag{41}$$

4. Experiments

A series of smooth round bar (SRB), notched round bars (NRBs) and shear samples were prepared for a wide range of stress states and different fracture mechanisms. Al-alloy 5052 was selected as the testing material, as it has good forming properties and is widely used in the manufacture of aircraft fuel tanks, electronic equipment panels, rivets and electrical enclosures. The chemical composition (wt.%) is shown in Table 1. The major alloying element is magnesium.

The geometry and dimensions of specimen are presented in Fig. 2. These samples with different geometrical constraints could ensure that the stress triaxiality varied with different fracture modes [7,8,14,16,18]. The tension tests were performed by an 100 kN INSTRON 1195 test machine at room temperature. The crosshead velocity was set as 0.3 mm/min for all specimens to ensure a quasi-static deformation. For the SRB and NRB samples, the longitudinal strain was measured using an extensometer over l_0 = 12.5 mm within the gauge section. The shear tests were performed by a compression apparatus which contains a punch, a container and a basement (see details in Fig. 3). This shear test setup is a new one which is different with the existing type in [7–10,13,14,16,18,37,38]. The load F and the displacement Δl were recorded and the characteristics are presented in Fig. 4. The

Table 1
The chemical composition of Al-alloy 5052 (wt.%).

Si	Fe	Cu	Mn	Mg	Cr	Zn	Ti	Al
0.08	0.19	0.02	0.02	2.36	0.18	0.03	0.01	Re

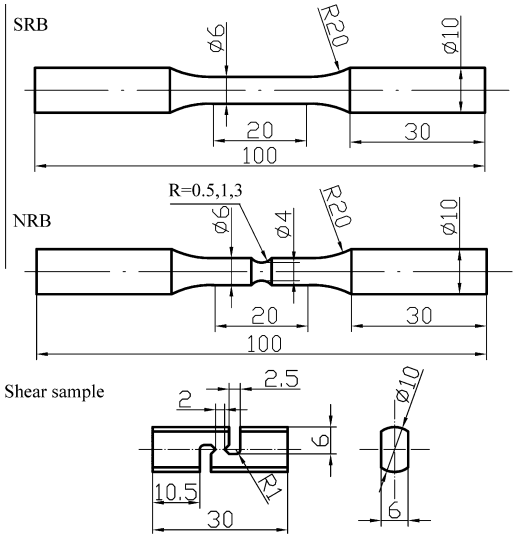

Fig. 2. Geometry and dimensions of the Al-alloy 5052 tensile samples and shear sample (in mm).

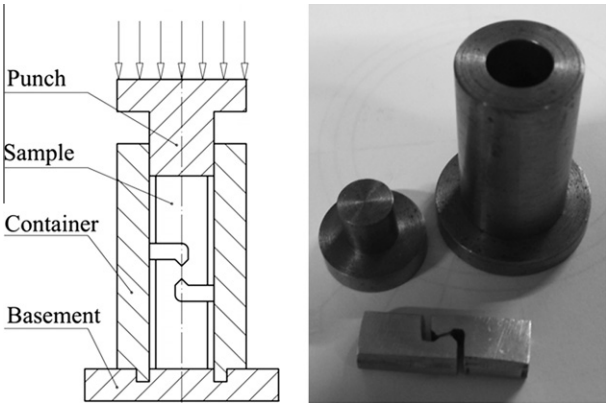

Fig. 3. The new experimental setup for shear test.

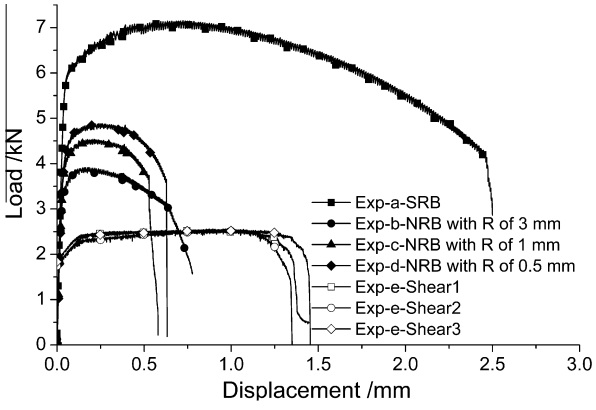

Fig. 4. Load–displacement curves from tensile and shear tests.

displacements at fracture of the NRB samples show decline compared with the SRB, in other word, showing the notch sensitivity of ductile materials, for higher stress triaxiality in notched round bars [7,18,39,40].

Fig. 5 shows the macroscopic fracture phenomenon by SEM fractographs, the cup-cone fracture mode was found in all of the

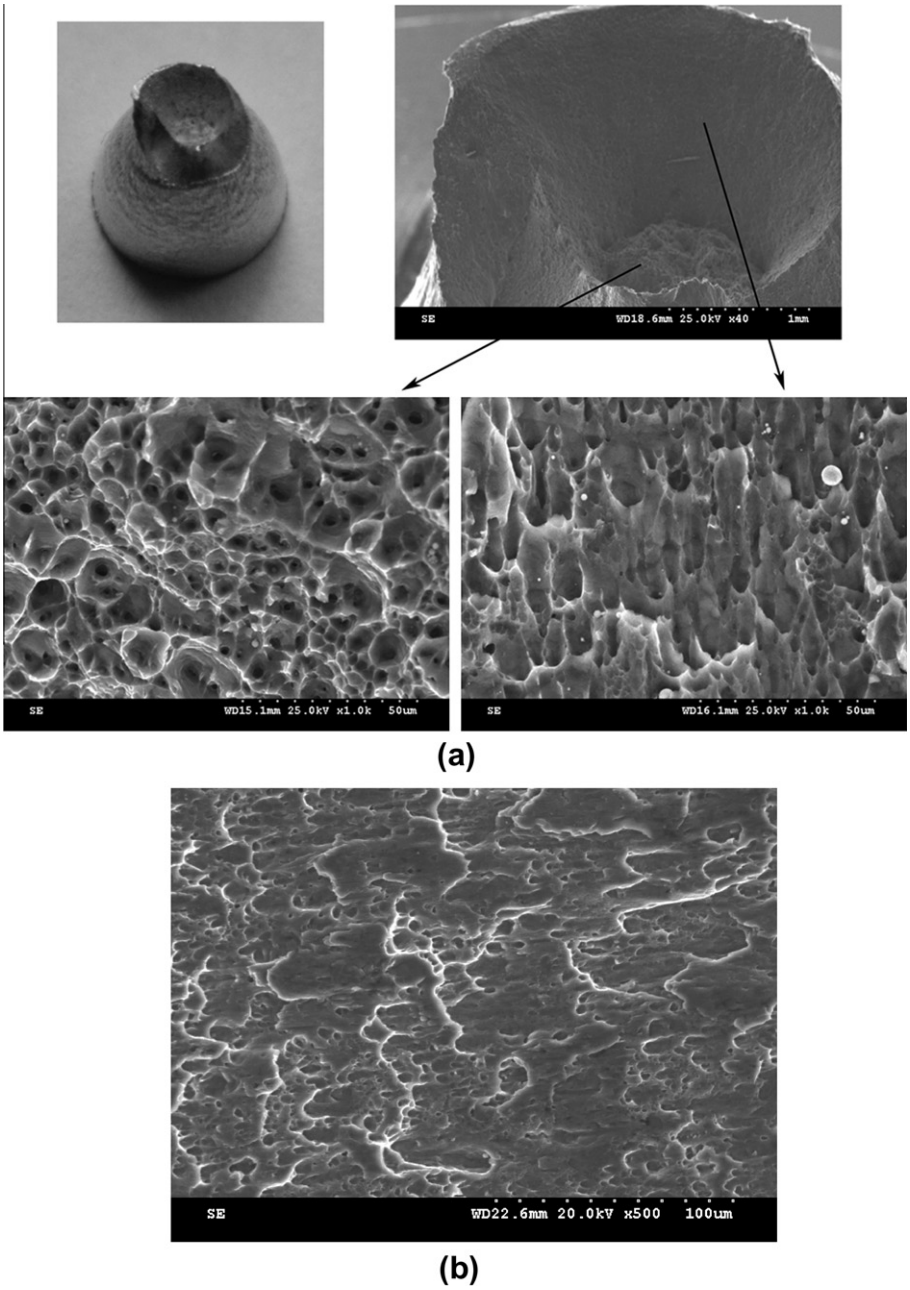

Fig. 5. (a) SEM fractographs of the SRB sample. Equi-axed ductile dimples can be found in the central region, while the cone region comprises highly elongated dimples. (b) SEM fractograph of the shear sample, elongated dimples do not cover the whole fracture surface like in the cone zone of (a).

SRB and NRB samples (Fig. 5a), similar to existing experimental results in [14,18,40]. Equi-axed ductile dimples can be found in the central region, while the cone region comprises highly elongated dimples, which indicates void coalescence by shear deformation. In Fig. 5b, it can be seen that for shear specimen, there are elongated dimples formed by void growth during shear deformation. The dimples do not cover the whole fracture surface like in the cone zone of Fig. 5a. Probably, in the shear localization region, a shear fracture mechanism combines with void deformation. Fig. 6 shows the longitudinal section of a sample which was not fully broken in experiment. By polishing it to the central section, the SEM fractograph shows the void distribution near the crack tip. We can see the void coalescence induced by shear and the crack propagation path. It can be seen that the crack occurs at the center and then grows radially. The transition from cup to cone is like branching and bifurcation.

5. Results and discussion

In this section, the main aims are to determine the material parameters such as the stress–strain curve in a wide range of plastic deformation and the damage-related parameters by a FE-based inverse calibration procedure combined with the physical experiments. The inverse procedure shows its potential in ductile fracture calibration [13–18]. Then the predictive ability of the modified Rousselier model is discussed by studying the cup-cone fracture mode in SRB and NRB samples. The material isotropy and strain-rate independence are assumed in the present study.

5.1. Determination of hardening model

The aim of this section is to obtain the stress–strain curve of Al-alloy 5052 from uniaxial tensile test of SRB sample. Then, the Voce

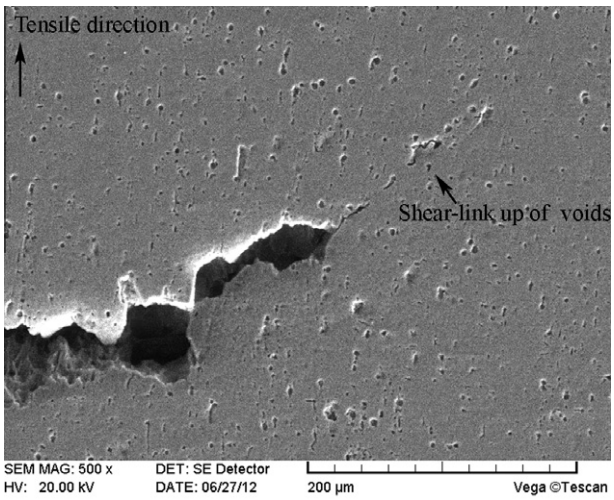

Fig. 6. The micrograph of the SRB sample section by SEM. The microvoids distribution near the crack tip shows the shear-link up of some voids.

hardening model is chosen to extend the stress–strain curve to a wide range of plastic deformation. The nominal strain ε_N is obtained by $\varepsilon_N = \Delta l/l_0$ and nominal stress by $\sigma_N = F/A$, where A is the section area of SRB sample. Prior to necking the true strain is given by $\varepsilon_T = \ln(1+\varepsilon_N)$, and the true stress by $\sigma_T = \sigma_N(1+\varepsilon_N)$. The stress–strain curves are presented in Fig. 7. This material shows uniform deformation, necking and fracture. For this material, the uniform deformation is small, so the Voce type hardening model is employed to fit the true stress–true strain curve to a wide range of plastic deformation [37,38] as the following equation:

$$R(p) = A - (A-B)\exp(-Cp) \tag{42}$$

Here, A, B, C are model constants. By least square fitting, the material constants are chosen as $A = 272.2$ MPa, $B = 209.6$ MPa and $C = 38.81$ respectively. The fitting results are also shown in Fig. 7.

5.2. Determination of σ_1 and D

According to [4], the material parameter σ_1 can be calibrated as

$$\sigma_1 = 2R(p_F)/3 \tag{43}$$

Here $R(p_F)$ is the equivalent stress when the fracture happens in smooth round bar tension test. By the Voce type hardening model as Eq. (42), the equivalent stress when the fracture happens can be obtained as $R(p_F) = A$. So the material parameter σ_1 can be determined as 180 MPa. The material parameter D is determined as 2 as in [4].

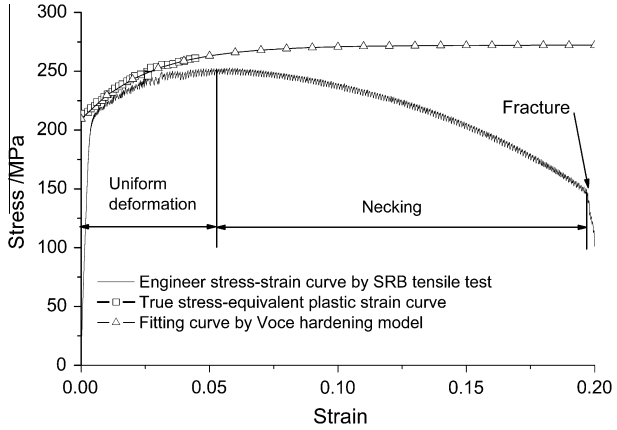

Fig. 7. The true stress–strain curve of Al-alloy 5052 at room temperature from tensile tests, and the fitting curve by the Voce hardening model.

5.3. Calibration for the initial void volume fraction f_0 and the critical void volume fraction f_c

The critical void volume fraction f_c is not really a parameter of the Rousselier model nor a coalescence criterion. Fracture initiates by strain localization because of the softening, f_c is only used in order to delete the element. According to the discussion in [3,21], the critical void volume fraction f_c at fracture can be chosen as 0.15 for this material and then the only unknown parameter is f_0. Usually, the void consists of brittle intermetallic phase in the aluminum alloys [4,41]. In order to identify the initial volume fraction of inclusions, metallographic investigation on polished surface of the specimens was performed. The results show that the initial void volume fraction f_0 is very low considering that the material is aluminum alloy. So in this section, the FE-based inverse fitting procedure in [3] is employed here to determine the initial void volume fraction f_0 as follows.

Three analyses were run first using the original Rousselier model, with initial void volume fraction $f_0 = 0.0001, 0.001, 0.005$ respectively. While the critical void volume fraction f_c is 0.15, in other words, when the void volume fraction in the material reaches f_c, fracture occurs. The Young's modulus E is 68.9 GPa and Poisson's ratio ν is 0.33. And the finite element mesh is presented in Fig. 8. The axisymmetric boundary condition is chosen to simplify the simulation and the element size was 60×30 μm, providing 50 elements across the gauge radius [2,14]. The element type is CAX4R provided by ABAQUS/Explicit, which is a bilinear axisymmetric and quadrilateral four-node element with reduced Gaussian integration. The movement of the crosshead is represented by a displacement boundary condition. In the following analyses, by using the critical void volume fraction, the crack

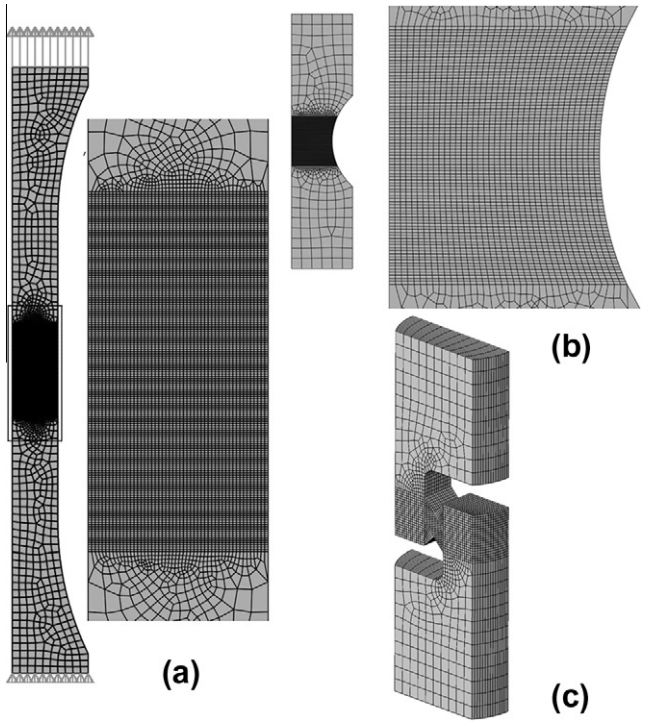

Fig. 8. The typical finite element meshes in simulations for the samples, (a) SRB sample with axisymmetric boundary condition, (b) NRB sample with axisymmetric boundary condition, and (c) shear sample with symmetric boundary condition.

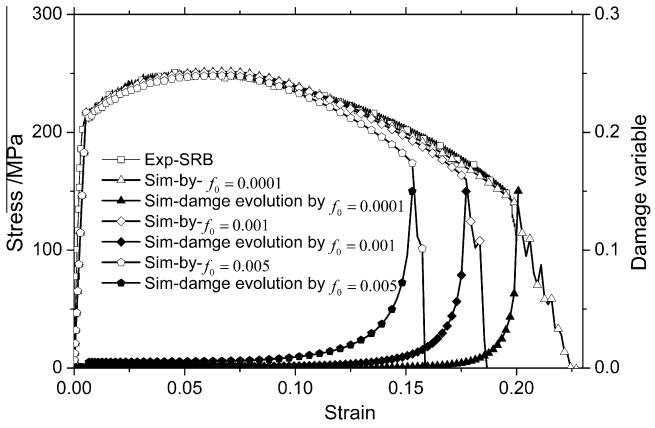

Fig. 9. The stress–strain curves and the evolutions of the damage variable versus engineer strain with different initial void volume fraction f_0 obtained by FEA using Rousselier model. The initial void volume fraction f_0 is calibrated as 10^{-4}. The critical void volume fraction f_c is chosen as 0.15.

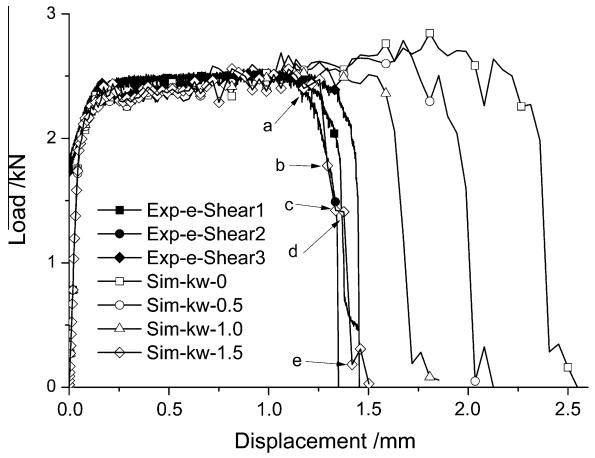

Fig. 10. Calibration procedure for shear damage coefficient k_ω by shear tests.

propagation is taken by element deletion [42]. In the FEA, when the state variable of the integral point reaches the threshold, the element will be deleted. And it is a popular way to simulate the evolution of 'crack' in the structures and widely used in recent researches as in [13,14,18,36,37]. And the engineer strain engineer stress curves were outputted and plotted in Fig. 9. The strain stress curves and the evolutions of the damage variable versus engineer strain obtained by simulations with different f_0 are also shown in Fig. 9. The damage variable increases monotonously with the deformation and the slope of the curve is very large in the end. And it can also be seen that, for $f_0 = 0.0001$, the difference between the simulation and experiment is acceptable and the damage variable evolution is in a reasonable range mentioned in other reference [2,3,5,14,21]. So, the initial void volume fraction f_0 was calibrated as 10^{-4} for this material. The simulation results also show that the Voce model in Eq. (42) can describe the plastic hardening behavior properly.

5.4. Determination of shear damage coefficient k_ω from shear tests

In order to verify the predictive ability of original Rousselier model under shear, an analysis was run for the shear test with $k_w = 0.0$. The FE mesh is presented in Fig. 8. Symmetric boundary condition is used and only half geometry is modeled. 3D eight-node brick elements with reduced Gaussian integration and hourglass section control (C3D8R in ABAQUS Explicit) were used in all regions. To improve computational efficiency, only the material in the shear region is modeled using the modified Rousselier model. Outside this zone the plate is modeled using standard von Mises plasticity model provided by Abaqus/Explicit. The minimum element size is 200 μm. Adaptive meshing is employed to avoid element distortion in the large localized shear deformation in the simulation. The other damage parameters are set as discussed above. Fig. 10 shows the displacement–load curve obtained by FE simulations. As shown in Fig. 10, for $k_w = 0$, the original Rousselier model can predict the failure of the material. But the displacement–load curve comparing with the experimental results shows that the ductility is over-estimated. In the original constitutive equations, the relation between the damage variable rate $\dot{f}$ with the volumetric plastic strain rate $\dot{\varepsilon}^p_m$ was derived by mass conservation as Eq. (6). So, the simulation results for shear deformation using the original damage evolution function do not agree with the experimental results.

As shown in Fig. 1, by assuming the initial void volume fraction f_0 and the critical void volume fraction f_c have already been estimated, the shear damage coefficient k_ω can be identified by shear tests. In order to determine the shear damage coefficient k_ω, other three analyses were run with $k_\omega = 0.5, 1.0, 1.5$ respectively. The displacement–load curve obtained by FE simulations are also shown in Fig. 10. It can be seen that, the larger the shear damage coefficient, the lower ductility obtained in simulation. We can see that by the modified model with shear damage coefficient $k_w = 1.5$, the ductility predicted by FE is closer to the physical

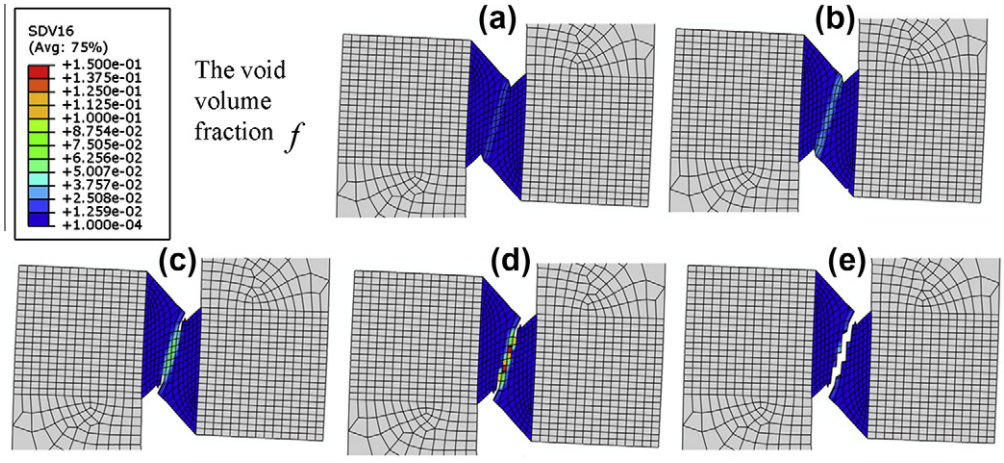

Fig. 11. The crack initiation and propagation predicted by the modified Rousselier model in shear tests were illustrated by the void volume fraction f when $k_\omega = 1.5$.

Table 2
Material parameters of Al-alloy 5052.

Model parameters	Value
Young's modulus E (GPa)	68.9
Poisson's ratio v	0.33
The Voce hardening model $\sigma = A - (A - B)\exp(-C\bar{\varepsilon}^p)$	
A (MPa)	272.2
B (MPa)	209.6
C	38.81
Rousselier parameter D	2
Rousselier parameter σ_1 (MPa)	180
Initial void volume fraction f_0	10^{-4}
Critical void volume fraction f_c	0.15
Shear damage coefficient k_ω	1.5

experiments, so the shear damage coefficient k_ω is calibrated as 1.5 for this material. In Fig. 11, the evolution of damage in simulation of shear test with $k_\omega = 1.5$ is shown. The crack initiation, propagation, and final failure in shear obtained by modified Rousselier model are also presented. The material parameters are summarized in Table 2.

5.5. Verification and discussion

To verify the predictive capability of the modified Rousselier model, several analyses were run to study the cup-cone fracture mode of SRB sample under tension. The predicted crack trajectory of the SRB sample under tension from FEA by modified Rousselier model is shown in Fig. 12 which indicates a cup-cone fracture mode. Fig. 12 shows the evolution of the damage variable and the invariant measure $\omega(\underline{\underline{\sigma}})$ of the stress for the SRB sample. We can see that the simulation results by the modified model can predict the fracture process of the specimen. First, the localization phenomenon occurs as a result of high triaxiality in the center. Then the porosity band branches to two shear bands, and the void

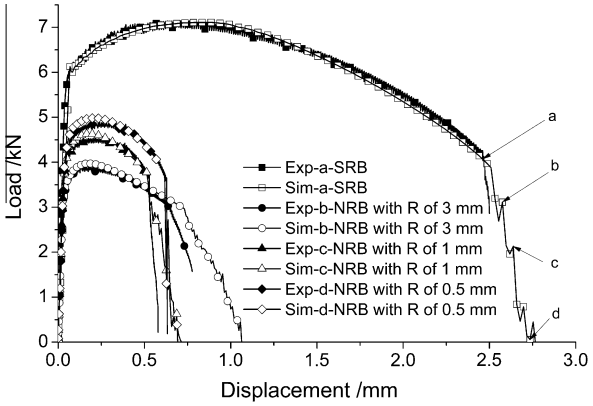

Fig. 13. Comparisons of the load–displacement curves from numerical simulations and experimental results.

evolution is influenced by shear localization. For the extended void evolution model incorporating shear, the void coalesce along the shear bands so that the crack propagates along one of the shear bands correspondingly resulting as bifurcation. When one of the bands is selected and the symmetry of the structure is lost, finally the ultimate fracture is cup-cone mode. We can see that for the modified Rousselier model, the new damage evolution function is influenced by the non-dimensional metric of stress state $\omega(\underline{\underline{\sigma}})$, so that the ductile damage evolution mechanisms under shear deformation can be described by the modified model. Fig. 13 presents the comparison of the load–displacement curves from numerical simulations with the experimental results. Good agreement can be found between the numerical and the experimental results. The points marked in Fig. 13 correspond to the stages (a) localization, (b) branching, (c) bifurcation and (d) fracture in Fig. 12.

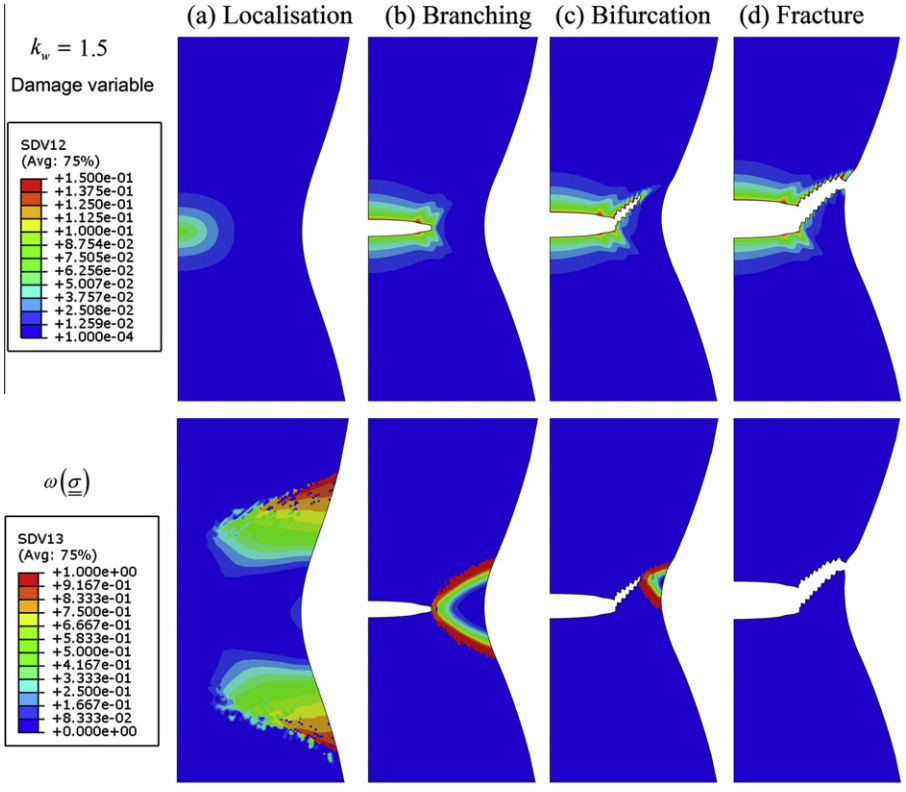

Fig. 12. The evolution of the damage variable and the invariant measure $\omega(\underline{\underline{\sigma}})$ of the SRB tensile sample by $k_\omega = 1.5$, when the crack grows to a certain length.

6. Conclusions

A modified Rousselier model which can predict shear failure as well as tension failure was proposed in this paper.

1. A recent extended damage evolution function considering a non-dimensional metric of stress state $\omega(\underline{\underline{\sigma}})$ with a shear damage coefficient k_ω was employed and a modified Rousselier model was proposed in this paper. A stress integration algorithm based on the return mapping method was given and implemented into finite element models using the user defined material subroutine VUMAT in the ABAQUS/Explicit platform.
2. The material parameters were calibrated by a finite element based inverse method. By uniaxial tension test, the initial void volume fraction f_0 and critical void volume fraction f_c were calibrated as 0.0001 and 0.15 for Al-alloy 5052 respectively. By a new type of shear test, the shear damage coefficient k_ω was calibrated as 1.5 for this material. The simulation results show that the modified model can give accurate results for the shear type failure.
3. The predictive capability of this model was carried out by studying the cup-cone fracture mode in the tensile tests. The validity of this model was verified by comparing the experiments with the simulations and good agreement was achieved. The results show that the new damage evolution function which is influenced by the metric of the stress can describe the void evolution mechanisms under shear deformation. So, the predictive ability of the modified Rousselier model was improved by the extended damage evolution model.

Acknowledgements

The authors would like to thank the reviewers for their constructive comments. The financial supports by the National Natural Science Foundation of China (No. 50975222), Research Fund for the Doctoral Program of Higher Education of China (20100201110002), and Double Degree Program of The University of Tokushima are gratefully acknowledged.

References

[1] A.L. Gurson, J. Eng. Mater. Technol. 99 (1977) 2–15.
[2] Arne S. Gullerud, Xiaosheng Gao, Robert H. Dodds Jr., R. Haj-Ali, Eng. Fract. Mech. 66 (2000) 65–92.
[3] Z.L. Zhang, C. Thaulow, J. Ødegård, Eng. Fract. Mech. 67 (2000) 155–168.
[4] Chang-Kyun Oh, Yun-Jae Kim, Jong-Hyun Baek, Young-Pyo Kim, Woosik Kim, Int. J. Mech. Sci. 49 (2007) 1399–1412.
[5] N. Benseddiq, A. Imad, Int. J. Pressure Vessels Pipings 85 (2008) 219–227.
[6] Jianqiang Chen, Yazid Madi, Thilo F. Morgeneyer, Jacques Besson, Comput. Mater. Sci. 50 (2011) 1365–1371.
[7] Yingbin Bao, Tomasz Wierzbicki, Int. J. Mech. Sci. 46 (2004) 81–98.
[8] Tomasz Wierzbicki, Yingbin Bao, Young-Woong Lee, Yuanli Bai, Int. J. Mech. Sci. 47 (2005) 719–743.
[9] I. Barsoum, J. Faleskog, Int. J. Solids Struct. 44 (2007) 1768–1786.
[10] Y. Bai, T. Wierzbicki, Int. J. Plast. 24 (2008) 1071–1096.
[11] Liang Xue, Tomasz Wierzbicki, Int. J. Solids Struct. 46 (2009) 1423–1435.
[12] K. Nahshon, J.W. Hutchinson, Eur. J. Mech. A – Solids 27 (2008) 1–17.
[13] K. Nahshon, Zhenyu Xue, Eng. Fract. Mech. 76 (2009) 997–1009.
[14] Z. Xue, M.G. Pontin, F.W. Zok, J.W. Hutchinson, Eng. Fract. Mech. 77 (2010) 492–509.
[15] K.L. Nielsen, V. Tvergaard, Eng. Fract. Mech. 77 (2010) 1031–1047.
[16] Matthieu Dunand, Dirk Mohr, J. Mech. Phys. Solids 59 (2011) 1374–1394.
[17] T.F. Morgeneyer, J. Besson, Scripta Mater. 65 (2011) 1002–1005.
[18] H. Li, M.W. Fu, J. Lu, H. Yang, Int. J. Plast. 27 (2011) 147–180.
[19] G. Rousselier, Nucl. Eng. Des. 105 (1987) 97–111.
[20] G. Rousselier, J. Mech. Phys. Solids. 49 (2001) 1727–1746.
[21] G. Rousselier, The Rousselier model for porous metal plasticity and ductile fracture, in: J. Lemaitre (Ed.), Handbook of Materials Behavior Models, vol. 2, Academic Press, San Diego, 2001, pp. 436–445.
[22] M. Springmann, M. Kuna, Comput. Mater. Sci. 26 (2003) 202–209.
[23] E. Lorentz, J. Besson, V. Cano, Comput. Methods Appl. Mech. Eng. 197 (2008) 1965–1982.
[24] M.K. Samal, M. Seidenfuss, E. Roos, B.K. Dutta, H.S. Kushwaha, Finite Elem. Anal. Des. 44 (2008) 358–371.
[25] M.K. Samal, M. Seidenfuss, E. Roos, B.K. Dutta, H.S. Kushwaha, Mater. Sci. Eng. A 496 (2008) 25–35.
[26] R. Bargellini, J. Besson, E. Lorentz, S. Michel-Ponnelle, Comput. Mater. Sci. 45 (2009) 762–767.
[27] M.K. Samal, M. Seidenfuss, E. Roos, Int. J. Mech. Sci. 51 (2009) 619–630.
[28] G. Rousselier, F. Barlat, J.W. Yoon, Int. J. Plast. 25 (2009) 2383–2409.
[29] G. Rousselier, F. Barlat, J.W. Yoon, Int. J. Plast. 26 (2010) 1029–1049.
[30] M. Seidenfuss, M.K. Samal, E. Roos, Int. J. Solids Struct. 48 (2011) 3365–3381.
[31] M. Zanganeh, C. Pinna, J.R. Yates, Int. J. Damage Mech., doi: 10.1177/1056789512441808.
[32] H.Y. Tu, S. Schmauder, U. Weber, Y. Rudnik, V. Ploshikhin, Eng. Fract. Mech. (2012), http://dx.doi.org/10.1016/j.engfracmech.2012.07.002.
[33] J.C. Simo, T.J.R. Hughes, Computational Inelasticity, Springer, New York, 1998.
[34] F. Dunne, N. Petrinic, Introduction to Computational Plasticity, Oxford University, New York, 2005.
[35] Jean Lemaitre, Rodrigue Desmorat, Engineering Damage Mechanics, Springer, New York, 2005.
[36] G. Rousselier, Finite deformation constitutive relations including ductile fracture damage, in: S. Nemat-Nasser (Ed.), 3D Constitutive Relations and Ductile Fracture, North-Holland Publishing Co., Amsterdam, 1981, pp. 319–343.
[37] A. Reyes, M. Eriksson, O.-G. Lademo, O.S. Hopperstad, M. Langseth, Mater. Des. 30 (2009) 596–608.
[38] E. Fagerholt, C. Dørum, T. Børvik, H.I. Laukli, O.S. Hopperstad, Int. J. Solids. Struct. 47 (2010) 3352–3365.
[39] P.W. Bridgman, Studies in Large Plastic Flow and Fracture, McGraw-Hill, New York, 1952.
[40] M.A. Meyers, K.K. Chawla, Mechanical Behavior of Materials, Cambridge University Press, New York, 2008.
[41] A. Ghahremaninezhad, K. Ravi-Chandar, Int. J. Fract. 174 (2012) 177–202.
[42] J. Mediavilla, R.H.J. Peerlings, M.D.G. Geers, Comput. Struct. 84 (2006) 604–623.